A Mathematical Model for Upper-Bound Analysis of Backward Extrusion in Ultra-Thin-Walled Tube Forming

Zahra Pahlevani and Ramin Ebrahimi (Corresponding Author: ebrahimy@shirazu.ac.ir)
Department of Materials Science and Engineering, School of Engineering, Shiraz University, Shiraz, Iran

Abstract

This study presents an analytical model based on the upper-bound method to investigate the backward extrusion of ultra-thin-walled tubes (wall thickness 100–400 μm). The deformation zone is divided into distinct regions with kinematically admissible velocity fields and defined discontinuities, allowing accurate estimation of strain rate field. The model incorporates effects of friction, wall thickness variation, and velocity discontinuities to predict extrusion force, deformation zone depth, and strain localization. Validation through both experimental measurements and finite element simulations demonstrates strong agreement with the analytical predictions. The proposed model offers an efficient and reliable framework for understanding deformation mechanics in precision tube extrusion and serves as a practical design tool in metal forming processes.

Keywords

Backward extrusion, ultra-thin-walled tubes, Upper-bound theory, Deformation mechanics, Frictional power, Strain localization

[DOI: 10.22068/ijmse.4600]

Nomenclature

Symbol	Description	Unit
R_0	Outer radius of the tube	mm
R_i	Inner radius of the tube (mandrel radius)	mm
$\boldsymbol{R_d}$	Outer radius of the billet	mm
$\boldsymbol{R_L}$	flow localization radius	mm
r	Radial coordinate	mm
$\boldsymbol{\theta}$	Circumferential direction	–
d	Mandrel diameter	mm
T	Depth of deformation zone	mm
h	Wall thickness of the tube	mm
L	Length of Container	mm
v_p	Punch velocity	mm/s
$\boldsymbol{v_f}$	Final material flow velocity	mm/s
$\boldsymbol{v_\theta}$	Velocity component in circumferential direction	mm/s
t	Deformation time	Sec
σ	Flow stress	MPa
$\bar{\sigma}$	Average flow stress	MPa
σ_m	Mean flow stress in deformation zone	MPa
$\dot{\varepsilon}$	Strain rate	s^{-1}
$\bar{\dot{\varepsilon}}$	Effective strain rate	s^{-1}
$\boldsymbol{d\varepsilon_H}$	Increment of homogeneous strain	–
m	Constant friction factor	–
k	Shear stress	MPa
k_0	Initial shear stress of material	MPa
$\boldsymbol{k_f}$	Final shear stress	MPa
$\boldsymbol{k_m}$	Mean shear stress	MPa
Δv	Velocity discontinuity	mm/s
S	Area of velocity discontinuity surface	mm^2
Γ	Velocity discontinuity surface	–
$\dot{W}$	Power consumption	W

[DOI: 10.22068/ijmse.4600]

1 Introduction

Ultra-thin-walled tubes, with wall thicknesses ranging from 100 to 400 microns, are increasingly in demand for applications in aerospace, medical devices, and micro-mechanical systems. These components are typically manufactured using high-reduction extrusion processes, which induce severe plastic deformation and result in concentrated strain within narrow deformation zones [1]. As tube wall thickness decreases, the surface-to-volume ratio increases, significantly amplifying frictional effects and promoting non-uniform deformation and redundant work. This presents a key challenge in precision tube forming at micron scales [2,3]. In this study, ultra-thin-walled tubes correspond to the tubes with wall thicknesses in the range of 100–400 μm and a wall-thickness-to-diameter ratio (h/D) of 0.08 or lower unless otherwise stated, this terminology is used consistently throughout the manuscript.

Backward extrusion is a widely adopted process for producing closed-end tubes, offering advantages such as high dimensional accuracy, excellent surface finish, reduced material waste, and minimized secondary operations [4]. Compared to forward extrusion, backward extrusion generally exerts lower frictional resistance and better accommodates complex geometries—making it ideal for ultra-thin-walled tube forming. However, as wall thickness decreases, the deformation mechanisms become more intricate, requiring advanced analytical and numerical modeling to predict extrusion force, deformation zone shape, and strain localization. Simulations by Tzou et al. [5] highlight how variations in friction, punch geometry, and wall thickness significantly influence velocity fields, flow patterns, and forming loads.

The Upper-Bound Method (UBM) provides a powerful analytical approach for metal forming processes. Based on kinematically admissible velocity fields and power dissipation minimization, UBM enables the estimation of forming loads and energy consumption without requiring full field solutions. Previous UBM-based studies have explored axisymmetric extrusion and tubes with complex geometries. While several models have addressed general extrusion processes [6], limited analytical efforts have focused specifically on ultra-thin-walled tubes in backward extrusion, where strain localization and friction-induced flow heterogeneity are prominent.

Initial analytical studies on backward extrusion focused on axisymmetric deformation using simplified velocity fields. Bae and Yang proposed upper-bound models for tubes with elliptic and complex internal geometries [4], while Abrinia and Gharibi extended the analysis to thin-walled cylindrical tubes via finite element simulation [2].

[DOI: 10.22068/ijmse.4600]

Research on magnesium alloy tubes Faraji et al. revealed that backward extrusion induces grain refinement and improved mechanical properties through severe plastic deformation [7]. Orangi and Abrinia further employed FEM to examine the influence of process parameters in tubes with arbitrary shapes [8].

On the theoretical side, generalized velocity fields introduced by Yang and Han [9], along with upper-bound analysis by Ebrahimi et al. [6], laid the groundwork for integrating strain-rate sensitivity and die geometry into extrusion models. Lee contributed UBM formulations for angular deformation processes involving discontinuous velocity fields [10], and Chang and Wang (2006) developed an optimized upper-bound formulation for axisymmetric extrusion through spherical dies, explicitly accounting for die geometry and frictional interfaces by employing a spherical velocity field model [11].

Recent research has extended the application of continuous velocity field formulations within UBM to better capture flow behavior in extrusion. For example, Bressan and Martins [12] analyzed axisymmetric extrusion using tailored streamline-based upper-bound solutions and compared them with finite-volume simulations. Similarly, Hong and Lou [13] developed upper-bound models for cold extrusion of box-shaped products using velocity fields responsive to varying die geometries and friction. Further advancements in SPD-based backward extrusion include techniques such as rotating backward extrusion (RBE), continuous extrusion, and other severe deformation methods, which enhance shear strain and promote microstructural refinement in thin-walled tubes, as demonstrated in recent experimental and FEM-based studies [14-16].

Further refinements to UBM have integrated discontinuous velocity surfaces, non-uniform strain fields, and mixed friction conditions [17–19]. Ebrahimi et al. [20] investigated forward–backward–radial extrusion via UBM, underscoring the role of strain path definition. Backward extrusion—particularly in variants such as rotating and accumulative backward extrusion—has proven to be an effective severe plastic deformation method, as validated through simulations and experiments [21,22]. Beyond conventional extrusion, the upper bound theory has also been extensively employed to analyze severe plastic deformation processes involving complex strain paths, such as equal-channel angular pressing [23,24].

Concurrently, the predictive accuracy of UBM has been substantiated through experimental and numerical studies across various tube extrusion settings [25,26]. For instance, Alexandrov et al. [27] presented a general upper-bound solution for axisymmetric extrusion and drawing, integrating die angle effects and frictional interactions in conical die systems. More recent

[DOI: 10.22068/ijmse.4600]

investigations addressed strain localization in thin-walled tubes, such as redundant strain buildup in flow forming [28] and hybrid UBM/velocity-field models for layered or curved profiles [29].

Despite significant advances in analytical and numerical modeling of extrusion processes, the deformation depth associated with strain localization in backward extrusion of ultra-thin-walled tubes has not, to the best of the authors' knowledge, been explicitly determined through analytical upper-bound formulations. In most existing studies, deformation depth and strain localization are inferred indirectly from numerical simulations or experimental observations. Furthermore, available analytical models largely focus on conventional tube thicknesses or simplified deformation modes and rarely provide quantitative insight into deformation zone depth, strain localization extent, or friction-dominated power consumption in ultra-thin-walled tubes, typically below 0.5 mm. Although numerical studies often report parametric trends, they generally do not offer closed-form relations that enable rapid estimation of extrusion force, deformation depth, and strain concentration across varying wall thicknesses and reduction ratios.

To address this gap, the present study proposes an upper-bound-based analytical model specifically tailored for the backward extrusion of ultra-thin-walled tubes. A physically motivated and kinematically admissible velocity field is adopted as a modeling assumption, enabling the analytical determination of deformation depth (T) directly through minimization of total power dissipation. This framework extends the applicability of upper-bound analysis beyond global force prediction toward explicit assessment of localized deformation behavior. The model incorporates segmented deformation zones, redundant strain, and mixed sliding–sticking friction conditions to predict extrusion force, deformation depth, and strain localization. Validation is performed through experimental measurements and finite element strain-field analysis. While the formulation is applicable to wall thicknesses in the range of 100–400 μm, experimental and numerical validation in the present work is conducted for the 400 μm case.

2 Methodology

In this section, an upper-bound analytical framework is developed to model the deformation behavior during backward extrusion of ultra-thin-walled tubes. This approach follows the classical variational principle by minimizing the total power dissipation through the use of kinematically admissible velocity fields, consistent with established formulations in extrusion modeling [30,31]. The deformation region is divided into multiple zones. Each zone is characterized by distinct flow patterns. Based on the works of Bae and Yang [4], and Ebrahimi et al. [20], curved or straight velocity discontinuity surfaces are introduced to model abrupt changes in material flow. Prager and Hodge's theoretical formulation for discontinuous velocity fields forms the basis for calculating power losses across these surfaces [32].

[DOI: 10.22068/ijmse.4600]

Referring to Figure 1 (a), the frictional conditions are modeled based on constant friction laws, where friction factors of m=0.1 on the all-frictional surfaces (AB, BC, FL, LQ, and AP), consistent with recent FEM studies applying constant friction models in pin-extrusion processes [33].

The total power consumption ($\dot{W}$) is evaluated as the sum of internal deformation power ($\dot{W}_i$), frictional power ($\dot{W}_f$), and velocity discontinuity power ($\dot{W}_\Gamma$), using the integral approach outlined by Druker [18] as follows:

$$\dot{W}_{tot} = \frac{2}{\sqrt{3}}\sigma_0 \int_V \sqrt{\frac{1}{2}\dot{\varepsilon}_{ij}\dot{\varepsilon}_{ij}}\, dV + \int_{S_\Gamma} k|\Delta v_\Gamma|\, dS + \int_{S_f} mk|\Delta v_f|\, dS - \int_{Si} T_i v_i dS \quad (1)$$

In the final step, the total power expression is minimized with respect to geometric or flow parameters, yielding an estimation of the required extrusion force. The validity of the proposed model is evaluated through direct comparison with experimental results obtained in this study, including force-displacement measurements and deformation observations. A close agreement between theoretical predictions and practical outcomes confirms the applicability of the upper-bound formulation to ultra-thin-walled backward extrusion. The formulation includes kinematically admissible velocity fields, strain rate estimation, and evaluation of power consumption. For clarity, full derivations of all mathematical expressions are provided in **Appendix A**, while only final relations are retained in this section.

2.1. Division of Deformation Zones and Velocity Field

As shown in **Figure 1 (a)**, the deformation region is divided into two primary subzones based on the observed material flow during backward extrusion:

- **Region I**: The central deformation zone located under the punch, where the material exhibits both axial (v_z) and radial (v_r) velocity components due to the compressive action of the punch.

[DOI: 10.22068/ijmse.4600]

- **Region II**: The surrounding flow zone in which the material is extruded radially and axially around the mandrel to form the ultra-thin-walled tube, also involving simultaneous v_z and v_r components.

Due to the axisymmetric condition of the process, the circumferential velocity component is assumed zero. Accordingly, the velocity field in both regions is assumed to contain two non-zero components: v_z and v_r which are defined to ensure continuity and incompressibility:

$$\frac{\partial v_z}{\partial z} + \frac{\partial v_r}{\partial r} + \frac{\partial v_\theta}{\partial \theta} = 0 \qquad (2)$$

The regions I and II, separated by a cylindrical velocity discontinuity surface AE. It is worth noting that the assumption of constant friction factor applies to the friction surfaces AB, BC, FL, LQ, and AP. Figure 1 illustrates the schematic view of the process and deformation model.

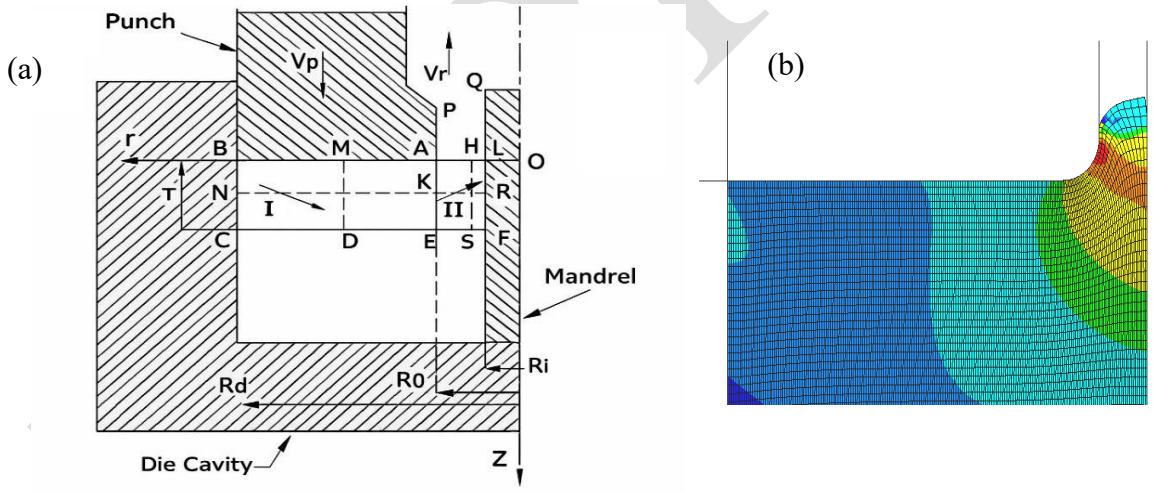

Figure 1: Schematic View of the Backward Extrusion Process: (a) Deformation model considered for the backward extrusion process of ultra-thin-walled tube, showing how the material moves in the deformation region, (b) Finite element mesh of the axisymmetric model showing local refinement in the deformation zone and near the die exit.

The adopted two-zone velocity field represents an idealized yet physically motivated approximation of the deformation pattern in backward extrusion of ultra-thin-walled tubes.

[DOI: 10.22068/ijmse.4600]

While localized strain heterogeneities may arise near sharp corners and contact interfaces, the formulation is designed to capture the dominant deformation mechanisms and associated power dissipation. The velocity field is kinematically admissible and analytically tractable, enabling material flow beneath the punch and within the radial deformation region to be described in a simplified form. Although it constitutes a modeling assumption within the upper-bound framework, its formulation allows the deformation depth T to be determined directly through minimization of total power dissipation, rather than being prescribed or inferred a posteriori.

The contact surfaces AP and LQ are defined by the intersections between the billet, punch, die, and mandrel and are fully determined by the billet radius, mandrel radius, punch contact, and wall thickness. Their lengths are obtained directly from the geometric relations shown in Fig. 1 (a) and are therefore not treated as independent parameters. It is worth noting that, the punch contact length is several times the tube thickness, which is sufficient to form the tube. The specific analytical forms of v_z and v_r used in this study are presented in **Appendix A**, where they are constructed to satisfy boundary conditions and kinematic admissibility in both regions.

The adopted velocity field, inclusion of velocity discontinuity surfaces, and explicit evaluation of frictional power on multiple interfaces are particularly important for ultra-thin-walled tubes, where high surface-to-volume ratio amplifies frictional effects and strain localization. In the finite element model, local mesh refinement is applied in the deformation zone and near the die exit to capture these high gradients. The final expressions for extrusion pressure, deformation zone depth (T), and total power consumption are summarized in Eqs. (4)–(7), whereas the detailed derivation steps are provided in Appendix A.

2.2. Strain Rate and Effective Strain Estimation

This strain rate is employed in estimating the internal power dissipation within the deforming zone. Based on the defined velocity fields, the components of the strain rate tensor and the effective strain rate ($\bar{\dot{\varepsilon}}$) were derived analytically (see Appendix A). The final expression used in calculations is:

$$\bar{\dot{\varepsilon}} = \sqrt{\frac{2}{3}\left(\dot{\varepsilon}_{rr}^{2} + \dot{\varepsilon}_{\theta\theta}^{2} + \dot{\varepsilon}_{zz}^{2}\right)} \tag{3}$$

This strain rate is employed in estimating the internal power dissipation within the deforming zone**.**

[DOI: 10.22068/ijmse.4600]

2.3 Force and Power Analysis

The billet material is modeled as isotropic elastic–plastic with strain hardening. The constitutive behavior is represented through a flow-stress relation in which the average flow stress is expressed as a function of the effective strain, $\overline{\sigma} = f(\overline{\varepsilon})$ (Appendix A, Eq. A.39). The effective strain is obtained from the kinematically admissible velocity fields and the associated strain-rate components described in Appendix A. The calculated average flow stress is subsequently employed in the evaluation of internal deformation power by integrating over the volumes of Regions I and II (Appendix A, Eq. A.40). The adopted material parameters correspond to the experimentally characterized response of annealed AA1050 aluminum alloy.

The total power consumed in the process is composed of three components:

- Internal deformation power $\dot{W}_i$
- Frictional power $\dot{W}_f$
- Velocity discontinuity power $\dot{W}_\Gamma$

Each of these terms is derived analytically in **Appendix A**, based on the geometry and surface conditions. Frictional behavior is modeled using constant friction laws, where friction factors of m=0.1 on the all-frictional surfaces.

The total power consumption is expressed as:

$$\dot{W}_{total} = \dot{W}_i + \dot{W}_f + \dot{W}_\Gamma \tag{4}$$

The extrusion force is obtained from:

$$F = \frac{\dot{W}_{tot}}{v_p} \tag{5}$$

Where v_p is the punch speed. According to Eq. (6) (see the Appendix A), The required pressure to perform the process is obtained as follows:

$$\dot{W}_{tot} = F.v_p = \pi\left({R_d}^2 - {R_0}^2\right)P_{Ext}v_p \tag{6}$$

(7)

[DOI: 10.22068/ijmse.4600]

$$P_{ext} = \frac{\sigma_{m_I}}{\sqrt{3}(R_d^2 - R_0^2)}\left[2R_d^2 - R_d^2\, log\sqrt{3} - \sqrt{3R_0^4 + R_d^4} + \frac{R_d^2}{2} log\left(\frac{\sqrt{3R_0^4+R_d^4}+R_d^2}{\sqrt{3R_0^4+R_d^4}-R_d^2}\right)\right] +$$

$$\frac{\sigma_{m_{II}}}{\sqrt{3}(R_0^2 - R_i^2)}\left[-2R_i^2 + R_i^2\, log\sqrt{3} + \sqrt{3R_0^4 + R_i^4} + \frac{R_i^2}{2} log\left(\frac{\sqrt{3R_0^4+R_i^4}-R_i^2}{\sqrt{3R_0^4+R_i^4}+R_i^2}\right)\right] +$$

$$\frac{1}{R_d^2 - R_0^2}\left[\begin{matrix} R_0(1+C)(k_{m_I}T + 2mk_fL_0) + \frac{(mk_{m_I} + k_0)}{T}\left(\frac{R_0^3 + 2R_d^3}{3} - R_0R_d^2\right) + mK_{m_I}R_dT + \\ mK_{m_{II}}CR_iT + 2mK_fCR_iL_{MN} \end{matrix}\right]$$

$$+\frac{1}{T(R_0^2 - R_i^2)}\left(\frac{R_0^3 + 2R_i^3}{3} - R_0R_i^2\right)(K_f + K_0)$$

The deformation zone depth T is obtained by minimizing the extrusion pressure with respect to T.

In required pressure, if the shape and dimensions of the die and punch and the constant friction factor between the tool and workpiece are known, all parameters except T are specified. Therefore, to calculate the pressure, we first need to determine the depth of the deformation region, represented by T. In the analytical formulation, billet diameter (d_0) and tube wall thickness are treated as parametric variables and are systematically varied in the parametric studies. the analysis performed for various billet radii in the range of 2.5-7 mm and wall thicknesses ranging from 0.1 to 3 mm in order to investigate the influence of initial billet size and wall thickness on deformation depth and strain localization.

2.4 Finite Element Simulation

Numerical simulations were carried out using the commercial finite element software ABAQUS/Explicit. A two-dimensional axisymmetric model was adopted due to the axisymmetric nature of the backward extrusion process. The billet was modeled as elastic–plastic material, while the die, punch, and mandrel were assumed rigid. A mesh sensitivity analysis was conducted using approximately 4500, 8000, and 13,000 elements. The mesh with about 8000 elements was selected. Therefore, the billet was discretized using approximately 8000 quadrilateral CAX4R elements, with mesh refinement concentrated in the deformation zone and

[DOI: 10.22068/ijmse.4600]

near the die exit. The punch was prescribed a constant downward velocity, while the die and mandrel were fixed. The finite element mesh and local refinement strategy are illustrated in Figure 1 (b). The plastic flow and frictional behavior of the material AA1050 aluminum alloy ($\sigma = 106\varepsilon^{0.349}\,MPa$ and μ=0.038) obtained from compression tests, were implemented in the software.

3 Experiment Procedure

Backward extrusion was chosen to reduce the high friction present in direct extrusion. The experimental setup and die used to produce ultra-thin-walled tubes with a 5 mm inner diameter and a 400-micron wall thickness is shown in Figure 2.

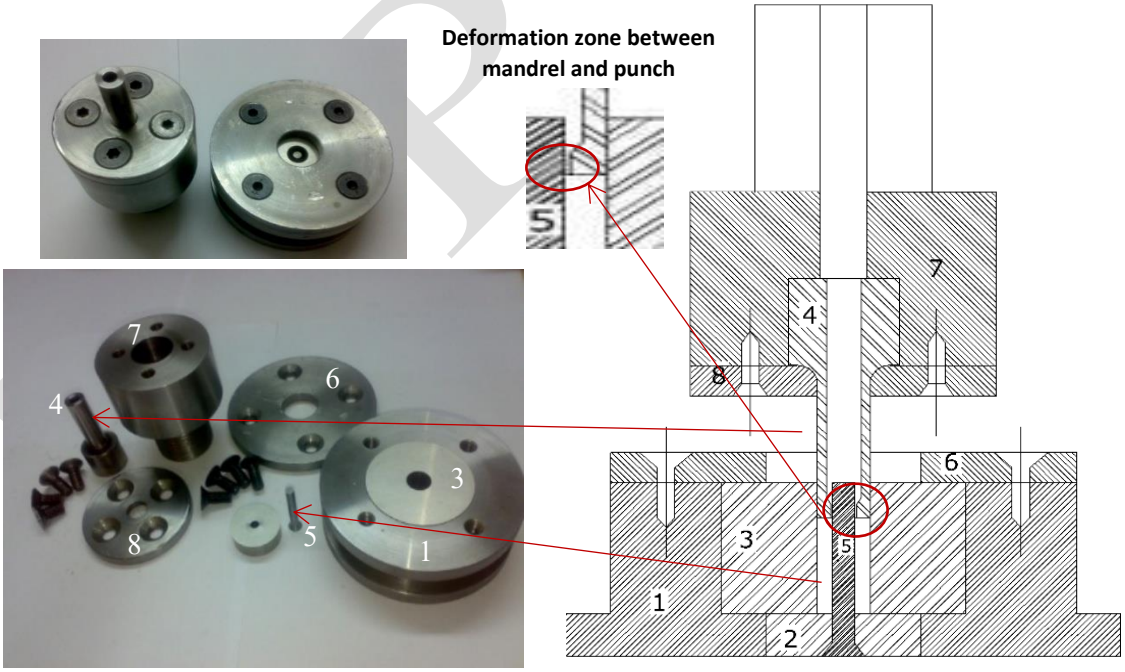

Figure 2: Backward extrusion die parts and assembly setup: Punch: No. 4, Punch holder: No.7&8, Die: No. 2 &3, Mandrel: No. 5, Die Holder:1,6

[DOI: 10.22068/ijmse.4600]

Die design- Die components, including the punch and mandrel, were made from SPK tool steel for its excellent hardenability and post-hardening strength (55 HRC). The internal punch edge was rounded to a 1.25 mm radius to ensure smooth material flow. A 3 mm contact length between the punch and mandrel was optimized to minimize friction and prevent misalignment.

Sample Preparation- Samples as initials billet were machined from AA1050 aluminum alloy into hollow cylinders. To relieve machining stresses, the samples were annealed at 600°C for three hours. The flow parameters used in the analytical and FE models were obtained by fitting compression test data of AA1050 aluminum alloy. Extrusion Setup- A 20-ton press with computer control was employed, operating at a ram speed of 0.2 mm/s. The ram displacement ensured a 2 mm residual at the billet's base for complete extrusion. The extrusion force was recorded using the built-in load cell of the screw press, which was connected to a computer system with a resolution of 0.01 kN. The deformation zone depth was measured from metallographic cross-sections using the scale bar on the optical micrographs. Lubrication- Various lubricants were tested, including graphite powder, MoS_2, SAE 40 oil, and Teflon. Teflon proved most effective in minimizing friction and preventing aluminum adhesion.

Cylindrical specimens of 10 mm diameter and 15 mm height were used for uniaxial compression tests, machined from the same AA1050 aluminum alloy billets. A constant cross-head speed of 0.2 mm/sec was applied.

4 Results and Discussion

4.1. Estimation of the Force in the Backward Extrusion Process of the Tube Based on the Proposed Model

The extrusion force was estimated using the upper-bound model presented (see Appendix A.41). Based on the optimized deformation zone geometry, the total power consumption was evaluated and converted into extrusion pressure, which was multiplied by the punch cross-sectional area to calculate the forming load. The force–displacement curve was generated by integrating the load along the punch stroke. Figure 3 illustrates the force-displacement curve of the punch, calculated by this method for billets with different diameters.

[DOI: 10.22068/ijmse.4600]

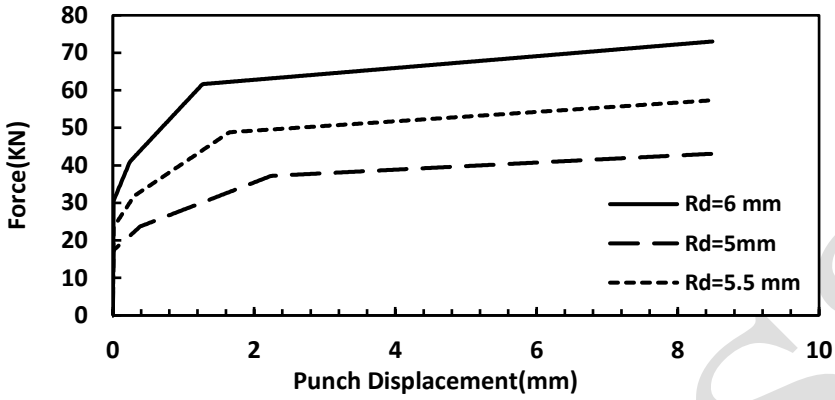

Figure 3: Force Variation with Punch Displacement Based on the Upper-Bound Model.

The experiment for the billet with an initial billet radius of 6 mm and a wall thickness of 400 μm was repeated three times. The average experimental peak force was 6.7 tons (Figure 4) with a deviation of ±0.15 tons. The comparison of the force-displacement graph obtained from the process with the predicted force by the upper-bound model is presented in Figure 4.

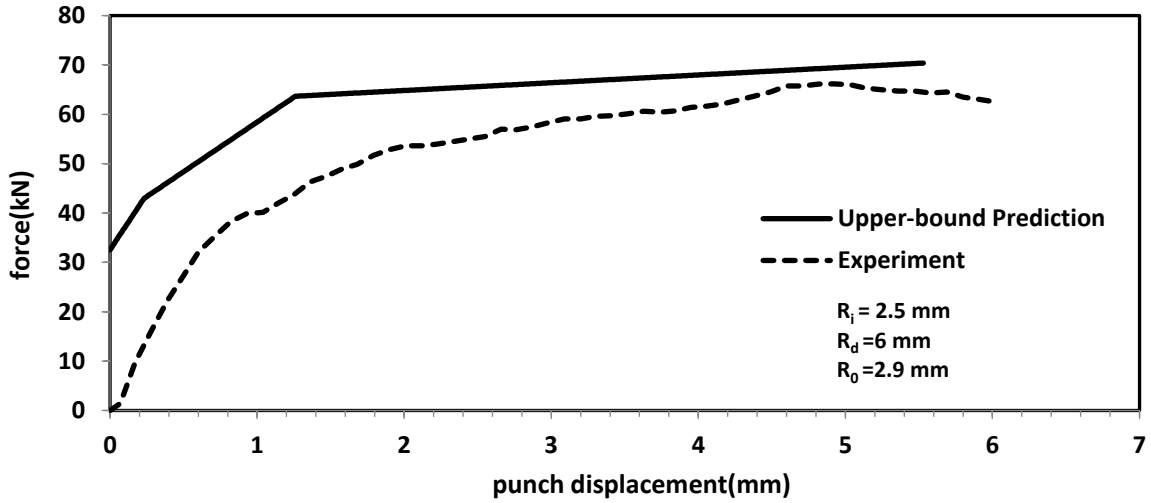

Figure 4: Comparison between analytical prediction and average experimental force–displacement curve for the 400 μm wall thickness tube.

[DOI: 10.22068/ijmse.4600]

After aligning the slope of the analytical force–displacement curve with the experimental curve, the absolute force values predicted by the analytical model are compared with the experimental results to assess the predictive capability of the model under the tested conditions. This level of agreement confirms the reliability of UBM predictions for backward extrusion of ultra-thin-walled tubes, in line with previous experimental validations [25–27] and its proven performance in more complex cases such as bi-metallic extrusion and non-axisymmetric profiles [34,35].

4.2. Frictional Power Consumption for Different Surfaces

Frictional power was calculated for each interface by evaluating the third integral in the upper-bound equation (See Appendix: equation A-41). It is well recognized that asperity flattening and the resulting evolution of real contact area play a critical role in influencing frictional behavior during metal forming, as discussed by Zwicker et al. [36]. However, in the present study, the constant friction factor is introduced as a calibration parameter such that only the slope of the analytical force–displacement curve matches that of the experimental curve, independent of any offset in force magnitude. After aligning the slopes, the absolute force values predicted by the analytical model are compared with the experimental data, enabling assessment of the model's capability to predict force levels under the tested conditions. It is emphasized that adopting a constant friction factor is a common simplifying assumption in upper-bound formulations to retain analytical tractability, and its limitation is acknowledged. Therefore, a constant friction factor ($m = 0.1$) is applied consistently across interfaces (AB, BC, FL, LQ, and AP).

As shown in Figure 5, surface LQ showed the highest frictional power consumption, followed by AP, due to higher relative velocities despite moderate area contact. High relative velocities near the die exit significantly amplify frictional power loss and promote local shear zones. These observations are consistent with previous reports on strain localization phenomena in backward extrusion of various Aluminum Shaped Section Tubes by Orangi et al, revealed pronounced strain localization in contact regions and sharp corners, attributed to friction-induced flow heterogeneity and local shear intensification [37].

[DOI: 10.22068/ijmse.4600]

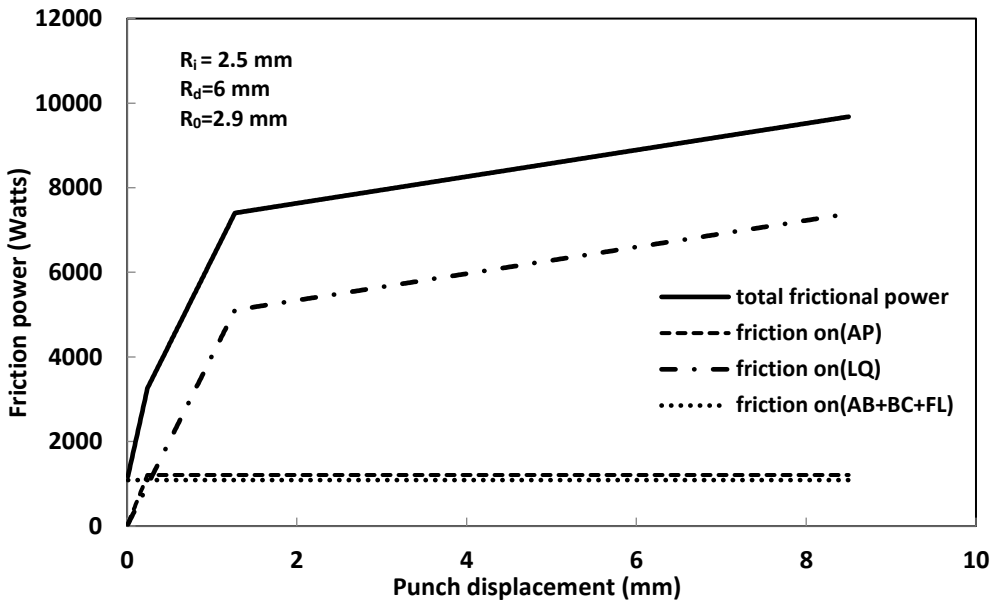

Figure 5: Comparing frictional power on each frictional surface for the 400 microns wall thickness produced tube.

The lengths of AP and LQ clearly affect the force calculation. However, since these lengths are assumed to be identical in the experiment, and analytical analysis, a direct comparison of the calculated forces is justified. However, these lengths do not affect the geometry of the deformation zone. Because they do not contribute to the upper-bound power optimization process.

4.3. Deformation Zone Depth Estimation

In the proposed upper-bound formulation, the deformation zone depth T is treated as an internal variable and is determined by minimizing the total power dissipation associated with the assumed velocity field. For the given geometry and process parameters, by solution of

[DOI: 10.22068/ijmse.4600]

$\frac{\partial}{\partial T}(P_{Ext}) = 0$, the depth of the deformation zone (T) is obtained as follows (Equation A.71 in Appendix A):

(6)

$$T^2 = \left[\left(R_d{}^2 - R_0^2\right) \frac{\frac{\left(\frac{R_0^3 + 2R_i{}^3}{3} - R_0 R_i^2\right)\left(k_f + k_0\right)}{\left(R_0^2 - R_i^2\right)} + \frac{\left(\frac{R_0^3 + 2R_d{}^3}{3} - R_0 R_d^2\right)\left(mk_{m_I} + k_0\right)}{\left(R_d^2 - R_0^2\right)}}{\left(\frac{mk_{m_{II}}(R_d^2 - R_0^2)Ri}{\left(R_0^2 - R_i^2\right)} + mk_{m_I} R_d + k_{m_I} R_0 \left(1 + \frac{R_d^2 - R_0{}^2}{R_0^2 - R_i^2}\right)\right)} \right]$$

For the experimental condition with an initial billet radius of 6 mm and a tube wall thickness of 400 μm, the analytical model predicts a deformation zone depth of approximately T ≈ 1.0 mm.

The deformation zone in metallographic images is identified based on the transition from heavily elongated grains to relatively undeformed regions along the extrusion direction, and the corresponding depth is estimated using the scale bar provided in the micrographs obtained by optical microscopy, in which the deformation depth is measured using the image scale bar, indicate a deformation depth of approximately T ≈ 1.2 ± 0.2 mm.

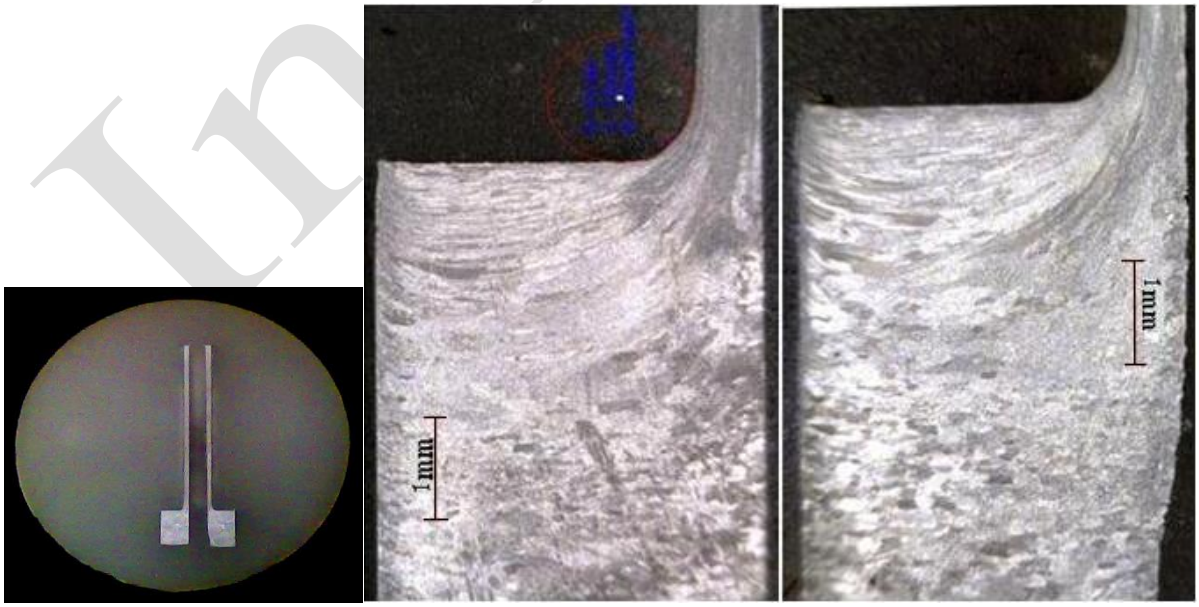

[DOI: 10.22068/ijmse.4600]

Figure 6: cross-sectional micrograph showing deformation zone of the 400 microns wall thickness produced tube (R_i = 2.5 mm, R_d=6 mm, R_0=2.9 mm).

The FEM-predicted deformation zone depth (Figure 11 (a)) was compared with metallographic observations (Figure 6). FEM results predict a deformation zone depth of approximately T ≈ 1.1 mm. which is in close agreement with that of metallographic measurement (T ≈ 1.2 ± 0.2 mm). The close proximity of these values indicates a consistent prediction of deformation zone depth by the analytical model, FEM simulation, and experimental observation.

The model assumes that the deformation depth corresponds to the point where the total power reaches a minimum, reflecting an energetically favorable state. This physically meaningful criterion enables the analytical estimation of plastic zone penetration depth without reliance on trial-and-error or numerical iteration.

For the investigated tube with a wall thickness of 0.4 mm, the deformation depth T predicted by the analytical model is in close proximity to the corresponding FEM prediction and to the value estimated from metallographic observations. The relative difference between these values is within approximately 10–15%, which is acceptable for upper-bound based analytical modeling of complex extrusion processes. This agreement indicates that the proposed velocity field provides a realistic representation of the deformation zone. According to experimental results and FEM analysis, the depth of the deformation zone — and in fact the boundary between the deformation zone and the undeformed zone — is not clearly observed as a sharp interface. However, in the present model, this boundary is assumed to be sharp, and the resulting predictions for the depth of the deformation zone are in reasonable agreement with both FEM and experimental observations.

4.4. Analysis of Factors Affecting the Depth of the Deformation Zone

A parametric analysis examined the influence of billet diameter, wall thickness, and friction factor, since these factors are variables affecting the depth of deformation (T) in the equation A.71 (Appendix A).

According to Figure 7: an increase in billet diameter led to deeper deformation zone, primarily due to increased reduction in area, with this effect being more pronounced for billets of smaller

[DOI: 10.22068/ijmse.4600]

initial diameters. The influence of wall thickness on the deformation depth exhibited a non-linear trend: as the thickness increased, the depth initially grew until reaching a critical threshold, beyond which it began to decrease due to the onset of flow localization. Figure 7(a) illustrates the variation of deformation zone depth for the 400 μm wall thickness tube under different area reductions. As billet radius increases, the reduction in area increases, requiring more material to flow radially outward. This larger volume of deforming material necessitates a deeper deformation zone to accommodate the strain gradient. The nonlinearity arises because the radial velocity gradient is inversely proportional to the square of the radius, leading to diminishing returns at larger diameters. In addition, Fig. 7(b) presents the variation of deformation zone depth over the entire ultra-thin-walled range (100–400 μm), showing a clear increase in deformation depth with increasing wall thickness. When the wall thickness exceeds approximately 2 mm, the deformation zone depth decreases after reaching a maximum, which signifies the development of strain localization near the punch. For thin walls (<1.5 mm), the deformation zone depth increases with wall thickness because the greater material volume absorbs energy through distributed plastic flow. However, beyond a critical thickness (~2 mm), the deformation depth decreases because the material can no longer sustain uniform flow; instead, strain localizes into a narrow shear band near the die exit. This transition is governed by the competition between radial flow constraint and frictional traction. Thicker walls reduce the axial-to-radial velocity ratio, promoting localized shear rather than deep penetration.

Moreover, a parametric study indicates that moderate variations in friction coefficient have only a minor influence on the deformation zone depth compared with geometric parameters. According to Figure 8, minimal impact on the deformation depth, suggesting that the process is predominantly governed by internal material flow rather than interface friction.

[DOI: 10.22068/ijmse.4600]

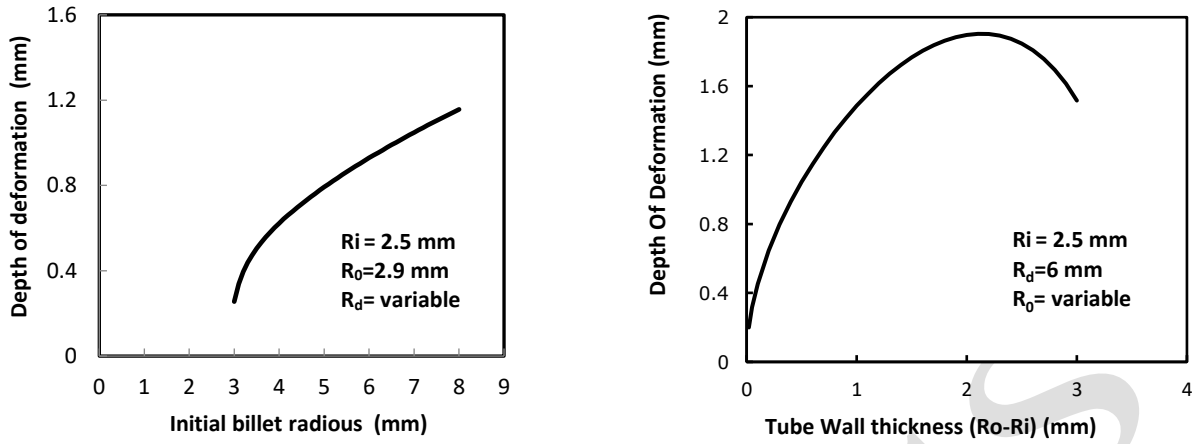

a b

Figure 7: Depth of deformation (T) vs. (a) Initial billet radius and (b) wall thickness.

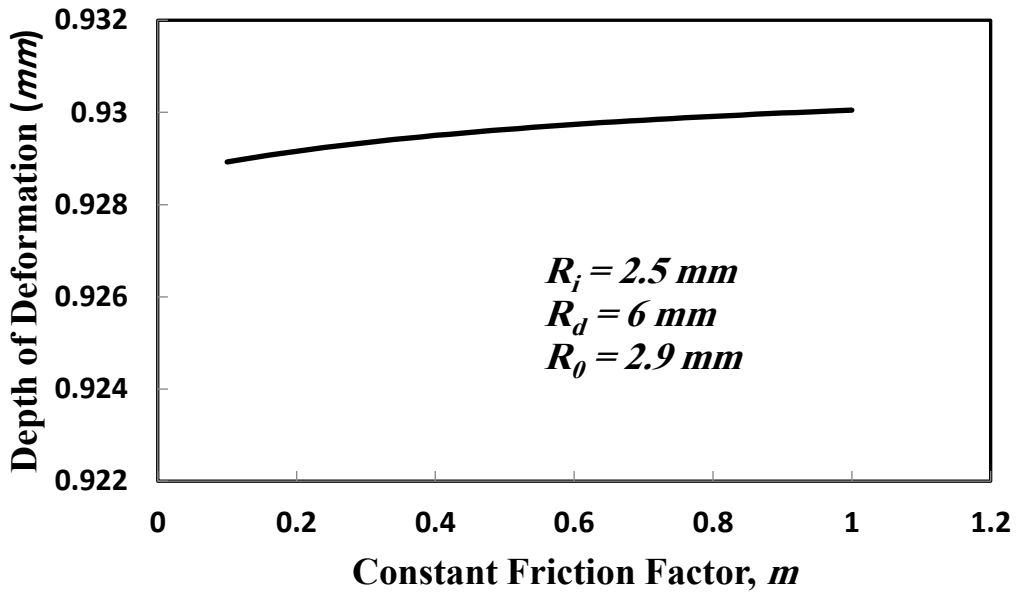

Figure 8: Insignificant variation of deformation zone depth with friction factor for the 400 μm wall thickness tube.

The value of *T* in the total frictional power consumption affects the size of the frictional surfaces BC and FL. According to Figure 5, the frictional contribution of these surfaces is very small compared to the two surfaces LQ and AP, where the material velocity is high. Therefore,

[DOI: 10.22068/ijmse.4600]

changing the frictional conditions (increasing m) causes a very small increase in the frictional power consumption on the surfaces BC and FL, which depend on the value of *T*. This has reduced the dependence of friction and the depth of the deformation zone. These findings highlight the sensitivity of *T* to geometry.

4.5. Strain Localization Region Based on the Proposed Model

Using the proposed analytical formulation, the location of strain localization in the radial direction was determined by evaluating the power consumption across varying radial distances in the shear zone (surface FL). For each assumed radius, **R**, between the mandrel and the tube outer radius, the total energy consumption was computed, and the point of minimum power was identified as the zone where strain localization occurs indicating with R_L (Figure 9).

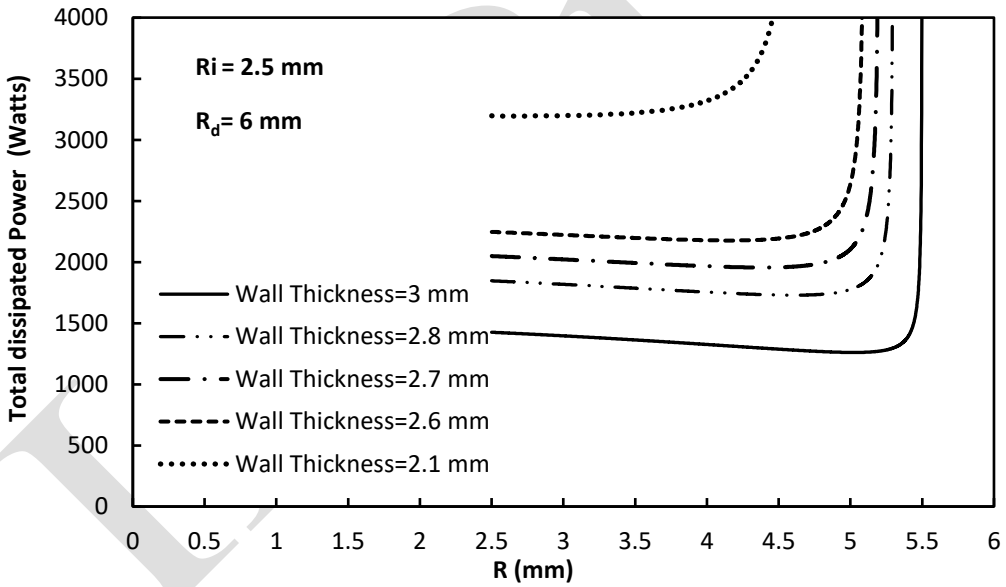

Figure 9: Power consumption vs. assumed shear surface R for different wall thicknesses.

The flow localization radius for different wall thicknesses, which are located after the maximum point on the curve in Figure 7 b, is obtained. Figure 10 shows how the flow localization distance changes with increasing tube wall thickness. This distance is the difference between the tube's

[DOI: 10.22068/ijmse.4600]

outer radius (R_0) and the flow localization radius (R_L) representing the thickness of the region where strain localization occurs.

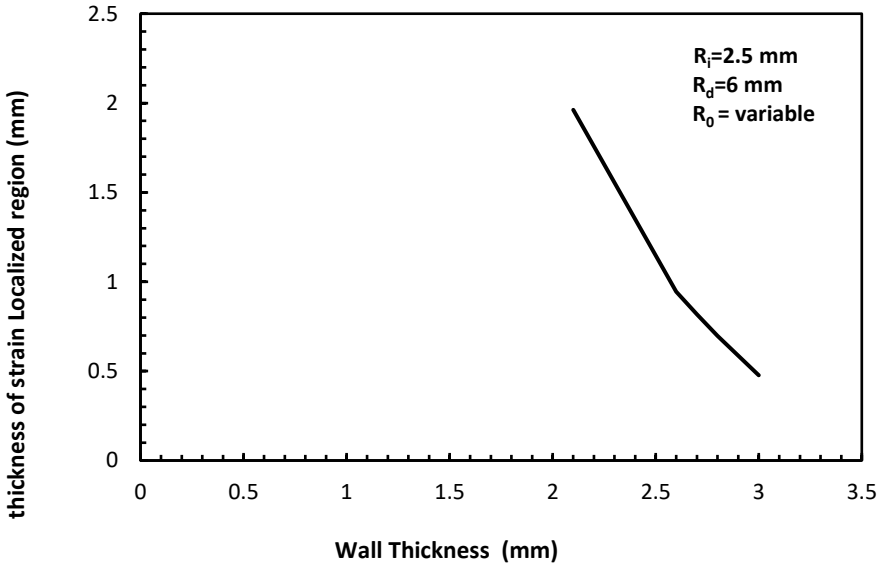

Figure10: Changes in the strain localization region thickness with increasing tube wall thickness.

As seen in the graph, increasing the wall thickness meaning decreasing in reduction in area, makes the strain localization region more localized and narrower. The occurrence of flow concentration is a process defect that causes material shear at the die exit. An investigation into the effect of the wall thickness of the produced tube on the depth of the deformation zone showed that, with excessive wall thickness, strain localization occurs early in the process.

To study strain localization, process simulations were conducted for tube production with wall thicknesses of 400 microns and 2.8 mm. According to Figure 7 (b), the wall thickness lies after the maximum point on the curve, so based on the calculations, producing a tube with this thickness will result in strain localization in the material. The radius of strain localization is the minimum point of the related curve in Figure 9 for each specified wall thickness tube. This point for the tube with wall thickness of 2.8mm is 4.603 mm accordingly. It means strain localization

[DOI: 10.22068/ijmse.4600]

begins at a distance of approximately 2.1 mm from the mandrel surface. Figure 11 shows equivalent strain distribution pattern and deformation zone depth after the process. According to FEM strain distribution pattern for the Given 2.8 mm wall thickness of the tube (Figure 11 b), the distance from the start of strain localization to the mandrel surface is about 2.1 mm so the radius of the strain localization (R_L) is approximately 4.6mm which is in a good agreement with that of the analytical calculation

Strain localization arises from the combination of high velocity gradients near the die exit and friction-induced shear at the LQ and AP interfaces. As wall thickness increases, the reduction in area decreases, causing the material to concentrate shear deformation in a narrow radial band rather than distributing it uniformly. The underlying mechanism is governed by the competition between geometric constraints (billet radius, wall thickness) and frictional traction. When the wall thickness exceeds a critical value (~2 mm in this study), the material near the outer radius undergoes intense local shear because the radial flow path becomes constrained, whereas thinner walls allow more uniform strain distribution.

So according to the proposed analytical approach, the radius of strain localization can be estimated for thicker tubes. As shown in Fig. 11(b), the analytically predicted localization radius exhibits good agreement with FEM results. For a tube with wall thickness of 2.8 mm, both analytical (Figure 9) and FEM models predict a localization radius of approximately 4.6 ± 0.1 mm from the tube axis. Small discrepancies between analytical and FEM-predicted strain localization originate from the idealized nature of the assumed velocity fields in the upper-bound model, which enforce uniform strain within each region. In contrast, FEM captures local heterogeneities and gradual strain gradients.

On the other hand, no strain localization is observed when the tube thickness is 400 microns (Figure 11 a), in agreement with that observation, the point correspond to this thickness is also located before the maximum point on the curve in Figure 7 b. Therefore, the simulation results align well with both the experimental and computational results derived from the proposed deformation model. In this regards strain localization in thick-walled tubes was localized near the outer radius, while thinner walls showed more uniform strain. The present analytical model identifies the onset and position of strain localization; however, explicit prediction of wrinkling or local buckling is beyond its current scope.

[DOI: 10.22068/ijmse.4600]

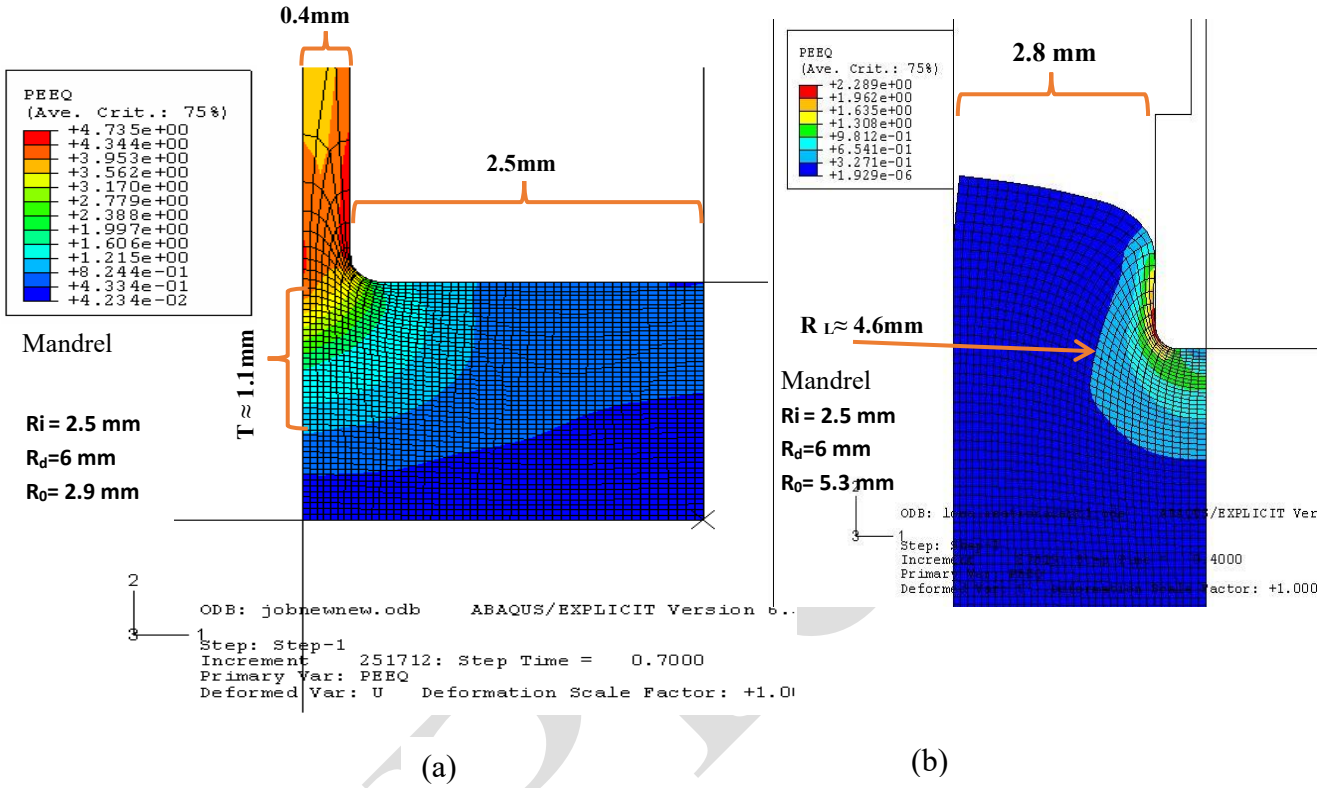

Figure 11: Equivalent plastic strain distribution from FEM simulations for (a) 400 μm wall thickness (uniform deformation, no localization) and (b) 2.8 mm wall thickness (localized shear near outer radius).

5 Conclusions

This work developed and validated an upper-bound analytical model tailored to the backward extrusion of ultra-thin-walled tubes. The main conclusions are as follows:

- The analytically predicted peak extrusion force (~7.3 tons) closely matched experimental results, confirming the reliability of the proposed model.
- Frictional power losses were most significant on surfaces with high velocity gradients (LQ and AP), consistent with simulation-based observations and highlighting the role of die-exit shear in strain localization.
- The calculated deformation depth (~1 mm) showed good agreement with both FEM simulations and metallographic measurements, validating the model's ability to capture localized plasticity.

[DOI: 10.22068/ijmse.4600]

- Deformation zone depth exhibited a strong nonlinear dependence on billet diameter and wall thickness, with minimal sensitivity to the friction coefficient—emphasizing the dominance of geometry over interface friction in this process.
- The model identified regions of strain localization based on energy dissipation analysis, which correlated well with FEM-derived strain fields. Thinner tubes showed more uniform deformation, while thicker walls promoted localized shear near the die exit.
- Compared with finite element simulations, which require several minutes per run, the analytical solution is obtained within seconds on a standard desktop computer, highlighting its suitability for rapid parametric analysis and preliminary process design.
- The analytically predicted extrusion force shows acceptable agreement with experimental measurements, while the analytically determined deformation depth exhibits consistent agreement with both metallographic observations and FEM-based strain-field analysis.
- The proposed framework is applicable within the investigated wall thickness range of 0.4–2 mm, as well as for larger wall thicknesses where localized deformation governs the backward extrusion behavior.
- Although experimental validation in the present study is limited to a single material and tool configuration, the generality of the analytical framework is demonstrated through extensive parametric analyses covering a range of wall thicknesses, billet radii, and reduction ratios. Since material work-hardening behavior influences deformation localization, further experimental investigations involving different materials and geometries are recommended to extend and strengthen the applicability of the proposed formulation.

Declarations

Acknowledgments

Financial support by the office of the Research Council of Shiraz University through grant number 99-GR-ENG 15 is appreciated.

Authors' contributions

Zahra Pahlevani: Conceptualization, Methodology, Formal analysis, Investigation, Writing – original draft.
Ramin Ebrahimi: Conceptualization, Supervision, Validation, Writing – review & editing, Project administration.
All authors reviewed the manuscript. All authors read and approved the final manuscript.

Funding

This research received no specific grant from any funding agency in the public, commercial, or not-for-profit sectors.

[DOI: 10.22068/ijmse.4600]

Competing interests

The authors declare that they have no known competing financial interests or personal relationships that could have appeared to influence the work reported in this paper.

Availability of data and materials

The datasets generated and analyzed during the current study are available from the corresponding author upon reasonable request.

Ethics approval and consent to participate

Not applicable.

Consent for publication

Not applicable.

6 References

1. Pahlevani Z, Ebrahimi R. Optimization of specific die profiles in thin-walled tube extrusion. *Iranian Journal of Science and Technology Transactions of Mechanical Engineering.* 2013; 37:203–215. https://doi.org/10.22099/ijstm.2013.1748
2. Abrinia K, Gharibi K. An investigation into the backward extrusion of thin-walled cans. *International Journal of Material Forming.* 2008;1: 411–414. https://doi.org/10.1007/s12289-008-0082-4
3. Peng Q, Dong H, Tian Y, Zhang H., Effect of backward extrusion on microstructure and mechanical properties of Mg–Gd based alloy. *Materials Science and Engineering A.* 2012; 532: 443–448. https://doi.org/10.1016/j.msea.2011.11.010
4. W.B. Bae, D.Y. Yang, An upper-bound analysis of the backward extrusion of internally elliptic-shaped tubes from round billets. *Journal of Materials Processing Technology.* 1992; 30:13–30. https://doi.org/10.1016/0924-0136(92)90036-R
5. Gow Yi Tzou, Chin Chuan Hsu, Ching Ting Kuo, FEM Simulation Comparisons of Backward Extrusion. *Advanced Materials Research*. 2012; 579: 42–51. https://doi.org/10.4028/www.scientific.net/AMR.579.42
6. Ebrahimi R, Reihanian M, Kanaani M, Moshksar MM. Upper-bound analysis of tube extrusion. *Journal of Materials Processing Technology*. 2008; 199: 214–220. https://doi.org/10.1016/j.jmatprotec.2007.07.034

[DOI: 10.22068/ijmse.4600]

7. Faraji G, Mashhadi MM, Kim HS. Microstructural evolution of UFG magnesium alloy by Accumulative Back Extrusion (ABE). *Material and Manufacturing Process*. 2012; 27(3): 267–272. https://doi.org/10.1080/10426914.2011.577880
8. K. Abrinia, S. Orangi. Investigation of process parameters for the backward extrusion of arbitrary-shaped tubes from round billets using finite element analysis. *Journal of Materials Engineering and Performance.* 2009; 18:1201–1208. https://doi.org/10.1007/s11665-009-9364-3
9. Yang DY, Han CH. A new formulation of generalized velocity field for axisymmetric forward extrusion through arbitrarily curved dies". *Trance ASME Journal of Engineering for Industry*. 1987; 109 (2): 161-168.
10. Dong Nyung Lee. An upper-bound solution of channel angular deformation. *Scripta Materialia.* 2000; 43 (2): 115-118. https://doi.org/10.1016/S1359-6462(00)00377-8
11. Der-Form Chang, Jyhwen Wang. Optimized Upper Bound Analysis of Axisymmetric Extrusion Using Spherical Velocity Field, *ASME Journal of Manufacturing Science and Engineering*. 2006; 128(1): 4–10. https://doi.org/10.1115/1.2112947
12. Jose Divo Bressan, Marcelo Mattos Martins. Study of Direct Metal Extrusion by the Upper-Bound and Finite Volume Methods. *Key Engineering Materials*. 2024; 987: 23–30. https://doi.org/10.4028/p-Ub1VHl
13. Hong Yan, Zhongming Lou. The upper-bound analysis of cold extrusion process for box-shaped products. *Materials Science and Engineering: B*. 2006; 132(1–2): 187-192. https://doi.org/10.1016/j.mseb.2006.02.021
14. Xin Che, Qiang Wang, Beibei Dong, Mu Meng, Zhiming Zhang. *Numerical and Experimental Analysis of Rotating Backward Extrusion as a New SPD Process*. *Metals and Materials International*. 2020; 26(12): 1786–1796. https://doi.org/10.1007/s12540-019-00600-z
15. Zhaoming Yan, Min Fang, Zhendong Lian, Zhimin Zhang, Jiaxuan Zhu, Guanshi Zhang, Yiding Wang. Research on AZ80 + 0.4%Ce (wt %) Ultra-Thin-Walled Tubes of Magnesium Alloys: The Forming Process, Microstructure Evolution and Mechanical Properties. *Metals.* 2019; 9, 563, https://doi.org/10.3390/met9050563

[DOI: 10.22068/ijmse.4600]

16. Xi Yang, Shihan Sun, Zheng Zhou, Xuewen Chen and Guoqing Chen. Continuous Extrusion Forming Technology of Magnesium Alloy Thin-Walled Tubules. *Materials*. 2023; 16, 5803, https://doi.org/10.3390/ma16175803
17. Philip G. Prager, William, Hodge. Theory of perfectly plastic solids. *John Wiley & Sons, Inc.,* 1951.
18. D.C. Drucker. Coulomb Friction plasticity and limit loads. *Journal of Applied Mechanics*. 1954; 21(1): 71-74. https://doi.org/10.1115/1.4010821
19. Wenbin Zhou, Zhusheng Shi, Jianguo Lin, Trevor A. Dean. An upper bound solution for deformation field analysis in differential velocity sideways extrusion using a unified stream function. *International Journal of Mechanical Sciences.* 2022; 224:107323. https://doi.org/10.1016/j.ijmecsci.2022.107323
20. A Farhoumand, R Ebrahimi. Analysis of forward–backward-radial extrusion process. *Materials & Design.* 2009; 30 (6), 2152-2157. https://doi.org/10.1016/j.matdes.2008.08.025
21. Yali Duan, Jianmin Yu, Beibei Dong, Huifang Zhang, Mu Meng, Mei Cheng, Zhimin Zhang, Baohong Zhang, Hongyuan Hao, Ping Xu, Huiling Liu. Microstructure Evolution and Dynamic Recrystallization Behavior of Mg-Gd-Y-Zn-Zr Alloy during Rotating Backward Extrusion. *Materials (Basel).* 2022; 15(3), 1057. https://doi.org/10.3390/ma15031057
22. S.M. Fatemi-Varzaneh, A. Zarei-Hanzaki. Accumulative back extrusion (ABE) processing as a novel bulk deformation method, *Materials Science and Engineering A.* 2009; 504: 104–106. https://doi.org/10.1016/j.msea.2008.10.027
23. M.H. Paydar , M. Reihanian, R. Ebrahimi, T.A. Dean, M.M. Moshksar, An upper-bound approach for equal channel angular extrusion with circular cross-section, 2008; 198(1-3), 48-53, https://doi.org/10.1016/j.jmatprotec.2007.06.051
24. M. Reihanian, R. Ebrahimi, M.M. Moshksar, Upper-bound analysis of equal channel angular extrusion using linear and rotational velocity fields, 2009; 30(1), 28-34, https://doi.org/10.1016/j.matdes.2008.04.059
25. H. Haghighat, M. Moradmand. An upper bound analysis of tube extrusion process through rotating conical dies. *Australian Journal of Mechanical Engineering*. 2013; 11(2): 111–120. https://doi.org/10.7158/M12-089.2013.11.2
26. H. Haghighat, M. Moradmand, Upper bound analysis of thick wall tubes extrusion process through rotating curved dies. *Meccanica*, 2013; 48(8): 1947–1958. https://doi.org/10.1007/s11012-013-9714-y

[DOI: 10.22068/ijmse.4600]

27. Sergei Alexandrov, Stanislav Strashnov, Yong Li. An Upper Bound Solution for Axisymmetric Extrusion and Drawing Considering a Generalized Yield Criterion. *Metals* 2023; *13*(3), 602. https://doi.org/10.3390/met13030602
28. M.S. Mohebbi, A. Akbarzadeh. Experimental study and FEM analysis of redundant strains in flow forming of tubes. *Journal of Materials Processing Technology. 2010; 210(2): 389-395.* https://doi.org/10.1016/j.jmatprotec.2009.09.028
29. H. Haghighat, H. Shayesteh. Upper bound analysis for hybrid sheet metals extrusion process through curved dies. *Transactions of Nonferrous Metals Society of China.* 2014; 20(14): 3285-3292. https://doi.org/10.1016/S1003-6326(14)63468-3
30. Haghighat H., Amjadian P. A generalized velocity field for plane strain backward extrusion through punches of any shape. *Meccanica*, 2013; 48: 2099–2106. https://doi.org/10.1007/s11012-013-9727-6
31. Wenbin Zhou, Jianguo Lin, Trevor A. Dean, Liliang Wang. Analysis and modelling of a novel process for extruding curved metal alloy profiles. *International Journal of Mechanical Sciences*. 2018; 138–139: 524–536. https://doi.org/10.1016/j.ijmecsci.2018.02.028
32. William Prager, Philip G. Hodge. Upper-bound solution for extrusion with velocity discontinuities. *Proceedings of the American Society of Civil Engineers.* 1950;76(1):1-10.
33. David Römisch, Martin Kraus, Marion Merklein. Tailored material flow in pin-extrusion of sheet metal under varying material and geometric conditions for enhanced joining technology applications. *International Journal of Material Forming*. 2025; 18:35. https://doi.org/10.1007/s12289-025-01897-5
34. H. Haghighat, G.R. Asgari. A generalized spherical velocity field for bi-metallic tube extrusion through dies of any shape, *International Journal of Mechanical Sciences.* 2011; 53(4): 248-253. https://doi.org/10.1016/j.ijmecsci.2011.01.005
35. Rong-Shean Lee, Chin Tarn Kwan. Upper-bound analysis for backward extrusion of generally non-axisymmetric hollow shapes. *Journal of the Chinese Society of Mechanical Engineers* (*Transactions of the Chinese Institute of Engineers*), *Series C*. 1997;18(2): 163–173.
36. Maximilian Zwicker, Niels Bay, Chris V. Nielsen1.A discussion of model asperities as a method to study friction in metal forming. *Discover Mechanical Engineering,* ۲۰۲۳; 2:3. https://doi.org/10.1007/s44245-023-00010-x

[DOI: 10.22068/ijmse.4600]

37. S. Orangi, K. Abrinia & R. Bihamta. Process Parameter Investigations of Backward Extrusion for Various Aluminum Shaped Section Tubes Using FEM Analysis. *Journal of Materials Engineering and Performance*. 2011; 20: 40–47. https://doi.org/10.1007/s11665-010-9655-8.

[DOI: 10.22068/ijmse.4600]

Appendix A – Derivation of Governing Equations in the Upper-Bound Model

A.1. Kinematically Admissible Velocity Field

To construct an admissible velocity field, it is assumed that the material deforms in two regions:

- **Region I (beneath the punch):** the material flows radially outward and axially downward.
- **Region II (around the mandrel):** the material flows radially backward and axially upward.

Due to axial symmetry, the circumferential velocity is zero:

The velocity field equation in regions I and II is assumed to contain v_z and v_r and are derived in the approach to satisfy volume constancy. These fields describe material flow in each region:

Region I:

$$v_{rI} = -\frac{{R_d}^2 - r^2}{2rT} v_p \tag{A.1}$$

$$v_{zI} = \frac{T - z}{T} V_p$$

$$v_\theta = 0$$

Region II:

$$v_{r\mathrm{II}} = -\left(\frac{r^2 - {R_i}^2}{2rT}\right)\left(\frac{{R_d}^2 - {R_0}^2}{{R_d}^2 - {R_i}^2}\right) v_p$$

$$v_{z\mathrm{II}} = -\frac{{R_d}^2 - {R_0}^2}{{R_0}^2 - {R_i}^2}\left(\frac{T - z}{T}\right) v_p \qquad \text{(A.2)}$$

$$v_\theta = 0$$

where:

- V_p is the punch velocity,
- R_0 is the initial billet radius,
- T is the deformation zone depth.

The above field satisfies the incompressibility condition:

$$\frac{\partial v_z}{\partial z} + \frac{\partial v_r}{\partial r} + \frac{\partial v_\theta}{\partial \theta} = 0 \qquad \text{(A.3)}$$

A.2. Strain Rate Tensor Components

From the velocity field, the non-zero strain rate tensor components are:

Strain rate tensors are derived from velocity fields for regions I and II. These tensors ensure the incompressibility condition, as shown in Equations (3)– (8).

A) Calculation of the strain rate tensor in the ***region*** **I**

$$\dot{\varepsilon}_{rr\mathrm{I}} = \frac{\partial v_r}{\partial r} = \left(\frac{{R_d}^2 + r^2}{2r^2 T}\right) v_p \qquad \text{(A.4)}$$

[DOI: 10.22068/ijmse.4600]

$$\dot{\varepsilon}_{zz\mathrm{I}} = \frac{\partial v_z}{\partial z} = \frac{-v_p}{T} \tag{A.5}$$

$$\dot{\varepsilon}_{\theta\theta\mathrm{I}} = \frac{v_r}{r} + \frac{1}{r}\frac{\partial v_\theta}{\partial \theta} = -\left(\frac{{R_d}^2 - r^2}{2r^2T}\right)v_p + \frac{1}{r}(0) = -\left(\frac{{R_d}^2 - r^2}{2r^2T}\right)v_p \tag{A.6}$$

As it can be seen $\dot{\varepsilon}_{rr} + \dot{\varepsilon}_{\theta\theta} + \dot{\varepsilon}_{zz} = 0$, therefore, Incompressibility condition, which is a necessary condition for the velocity field to be acceptable, is established. Now we will discuss the rest of the components of the strain rate tensor:

$$\dot{\varepsilon}_{r\theta\mathrm{I}} = \frac{1}{2}\left(\frac{1}{r}\frac{\partial v_r}{\partial \theta} + \frac{\partial v_\theta}{\partial r} - \frac{v_\theta}{r}\right) \Rightarrow \dot{\varepsilon}_{r\theta} = 0 \tag{A.7}$$

$$\dot{\varepsilon}_{\theta z\mathrm{I}} = \frac{1}{2}\left(\frac{\partial v_\theta}{\partial z} + \frac{1}{r}\frac{\partial v_z}{\partial \theta}\right) \Rightarrow \dot{\varepsilon}_{\theta z} = 0 \tag{A.8}$$

$$\dot{\varepsilon}_{zr\mathrm{I}} = \frac{1}{2}\left(\frac{\partial \dot{v}r}{\partial z} + \frac{\partial v_z}{\partial r}\right) \Rightarrow \dot{\varepsilon}_{zr} = 0 \tag{A.9}$$

B) Calculation of strain rate tensor in the region II

$$\dot{\varepsilon}_{zz\mathrm{II}} = \frac{\partial v_z}{\partial z} = \frac{v_p}{T}\left(\frac{{R_d}^2 - {R_0}^2}{R_0^2 - R_i^2}\right) \tag{A.10}$$

$$\dot{\varepsilon}_{rr\mathrm{II}} = \frac{\partial v_r}{\partial r} = -\left(\frac{{R_d}^2 - {R_0}^2}{{R_0}^2 - {R_i}^2}\right)\left(\frac{r^2 + {R_i}^2}{2r^2T}\right)v_p \tag{A.11}$$

$$\dot{\varepsilon}_{\theta\theta\mathrm{II}} = \frac{v_r}{r} + \frac{1}{r}\frac{\partial v_\theta}{\partial \theta} = -\left(\frac{{R_d}^2 - {R_0}^2}{{R_0}^2 - {R_i}^2}\right)\left(\frac{r^2 - {R_i}^2}{2r^2T}\right)v_p \tag{A.12}$$

[DOI: 10.22068/ijmse.4600]

$$\dot{\varepsilon}_{r\theta\mathrm{II}} = \frac{1}{2}\left(\frac{1}{r}\frac{\partial v_r}{\partial \theta} + \frac{\partial v_\theta}{\partial r} - \frac{v_\theta}{r}\right) \Rightarrow \dot{\varepsilon}_{r\theta} = 0 \tag{A.13}$$

$$\dot{\varepsilon}_{\theta z\mathrm{II}} = \frac{1}{2}\left(\frac{\partial v_\theta}{\partial z} + \frac{1}{r}\frac{\partial v_z}{\partial \theta}\right) \Rightarrow \dot{\varepsilon}_{\theta z} = 0 \tag{A.14}$$

$$\dot{\varepsilon}_{zr\mathrm{II}} = \frac{1}{2}\left(\frac{\partial \dot{v}r}{\partial z} + \frac{\partial v_z}{\partial r}\right) \Rightarrow \dot{\varepsilon}_{zr} = 0 \tag{A.15}$$

A.3. Effective Strain Rate

A) Estimation of homogeneous strain

Homogeneous and effective strains are estimated using deformation mechanics principles. The effective strain rate is derived as a function of strain tensor components. The homogeneous strain distributions for the extrusion of a tube are calculated as follows:

$$d\varepsilon_x = \frac{dA}{A} = \frac{d+2h}{h(d+h)}dh \tag{A.16}$$

$$d\varepsilon_y = \frac{-dh}{h} \tag{A.17}$$

$$d\varepsilon_z = \frac{-ds}{s} = \frac{-dh}{d+h} \tag{A.18}$$

A is the cross-sectional area of the cylindrical billet in the deformation zone, and *s* is the sum of the perimeter of this base and the perimeter of the inner cavity of the billet. Additionally, *d* is the mandrel diameter, and *h* is the wall thickness of the tube at the mid-point of the deformation zone. In this way, the equivalent homogeneous strain development ($d\varepsilon_H$) for the tube extrusion process would be as:

[DOI: 10.22068/ijmse.4600]

$$d\varepsilon_H = \frac{2}{\sqrt{3}}\left[\frac{3h^2 + 3hd + d^2}{h^2(h+d)^2}\right]^{\frac{1}{2}} dh \tag{A.19}$$

So, the Homogeneous strain in indirect extrusion would be obtained as follows:($h_f = R_0 - R_i$ & $h_0 = R_d - R_i$)

$$\varepsilon_H = \int_{h_0}^{h_f} d\varepsilon_H \tag{A.20}$$

The desired dimensions in this research are as follows: $R_0 = 2.9mm$ ،$R_d = 6mm$ ،$R_i = 2.5mm$.

According to the relation (19) and the above dimensions, the amount of homogeneous strain for the process was equal to 2.81.

B) Estimation of Total Strain in the Process

The von Mises equivalent strain rate is expressed as:

$$\bar{\dot{\varepsilon}} = \sqrt{\frac{2}{3}\left(\dot{\varepsilon}_{rr}^{2} + \dot{\varepsilon}_{\theta\theta}^{2} + \dot{\varepsilon}_{zz}^{2}\right)} \tag{A.21}$$

Substituting from Eqs. (A.4) – (A.15):

Therefore, the effective strain rate in zone I will be:

$$\bar{\dot{\varepsilon}}_I = \frac{v_p}{\sqrt{3}Tr^2}\sqrt{3r^4 + {R_d}^4} \tag{A.22}$$

Assuming: $C = \frac{R_d^2 - R_0^2}{R_0^2 - R_i^2}$, similarly, the effective strain rate in zone IIwill be:

[DOI: 10.22068/ijmse.4600]

$$\bar{\dot{\varepsilon}}_{II} = \frac{C v_p}{\sqrt{3} T r^2} \sqrt{3r^4 + {R_i}^4} \tag{A.23}$$

As shown, both $\bar{\dot{\varepsilon}}_{II}$ and $\bar{\dot{\varepsilon}}_{I}$ are functions of r; therefore, to calculate the effective strain, an average value for the effective strain rate must be determined:

$$\bar{\dot{\varepsilon}}_m = \frac{\int \bar{\dot{\varepsilon}} \ dV}{\int dV} \tag{A.24}$$

The differential volume element for zone I is calculated as follows, with r varying from R_0 to R_d:

$$dV = 2\pi r T dr \tag{A.25}$$

By substituting equations (24) and (21) into (23) and solving, the average effective strain rate is obtained as:

$$\bar{\dot{\varepsilon}}_{Imean} = \frac{2R_d^2 - R_d^2 \, log(\sqrt{3}) - \sqrt{3R_0^4 + R_d^4} + \frac{{R_d}^2}{2} log\left(\frac{\sqrt{3R_0^4 + R_d^4} + R_d^2}{\sqrt{3R_0^4 + Rd^4} - {R_d}^2}\right)}{\sqrt{3} T (Rd^2 - R_0^2)} v_p \tag{A.26}$$

Similarly, in zone II, the volume element is calculated as follows, with r varying from R_i to R_0:

$$dV = 2\pi r T dr \tag{A.27}$$

[DOI: 10.22068/ijmse.4600]

By substituting equations (26) and (22) into (23) and solving, the average effective strain rate in zone II is obtained as:

(A.28)

$$\bar{\dot{\varepsilon}}_{IImean} = \frac{v_p\left({R_d}^2 - R_0^2\right)\left[\sqrt{3R_0^4 + R_i^4} + R_i^2\, log(\sqrt{3}) - 2R_i^2 + \frac{R_i^2}{2} log(\frac{\sqrt{3R_0^4 + R_i^4} - R_i^2}{\sqrt{3R_0^4 + R_i^4} + R_i^2})\right]}{\sqrt{3}T(R_0^2 - R_i^2)^2}$$

The time it takes for the material to pass through the plastic deformation zone equals the time required for the punch to move a volume of material equal to the volume of the deformation zone.

$$\Delta z_p \pi\left({R_d}^2 - R_0^2\right) = \int dV \tag{A.29}$$

where Δz_p is the displacement of the punch needed to move a volume of material equal to the deformation zone. The plastic deformation time can be calculated by dividing the punch displacement Δz_p by its speed v_p. By numerically solving equation (A.29) for the deformation zone *I*, we can write:

$$t_I = \frac{\Delta z_p}{v_p} = \frac{T}{v_p} \tag{A.30}$$

Similarly, for the deformation zone II, we have:

$$t_{II} = \frac{\Delta z_p}{v_p} = \frac{R_0^2 - R_i^2}{R_d^2 - R_0^2}\frac{T}{v_p} \tag{A.31}$$

[DOI: 10.22068/ijmse.4600]

As mentioned earlier, effective strain is obtained by multiplying the average effective strain rate by the deformation time. By multiplying equation (A.30) by equation (A.26) for zone *I*, we get:

$$\bar{\varepsilon}_I = \frac{2{R_d}^2 - {R_d}^2 \log(\sqrt{3}) - \sqrt{3R_0^4 + R_d^4} + \frac{{R_d}^2}{2} \log\left(\frac{\sqrt{3R_0^4 + {R_d}^4} + R_d^2}{\sqrt{3R_0^4 + {R_d}^4} - R_d^2}\right)}{\sqrt{3}(R_d^2 - R_0^2)} \tag{A.32}$$

For the experimental dimensions, this value is obtained as 1.05. Similarly, by multiplying equation (A.31) by equation (A.28) for zone II, we get:

$$\bar{\varepsilon}_{II} = \frac{\sqrt{3R_0^4 + R_i^4} + R_i^2 \log\sqrt{3} - 2R_i^2 + \frac{{R_i}^2}{2} \log\left(\frac{\sqrt{3R_0^4 + R_i^4} - R_i^2}{\sqrt{3R_0^4 + R_i^4} + R_i^2}\right)}{\sqrt{3}(R_0^2 - R_i^2)} \tag{A.33}$$

For the experimental dimensions, this value is obtained as 1.

The shear strain caused by the passage of material across a velocity discontinuity surface can be interpreted as the ratio of the tangential velocity to the normal velocity relative to this surface [10]. According to the deformation model presented (Figure 1), using this concept, the shear strain on the two velocity discontinuity surfaces AE and AL is calculated as follows:

$$\gamma_{AE} = \frac{(T - z)2R_0\left({R_d}^2 - {R_i}^2\right)}{\left({R_d}^2 - {R_0}^2\right)\left({R_0}^2 - {R_i}^2\right)} \tag{A.34}$$

Considering the dependency of shear strain on z on this surface, the average strain value in the range of z from *0* to *T* is obtained as:

[DOI: 10.22068/ijmse.4600]

$$\gamma_{AE_{mean}} = \frac{TR_0\left({R_d}^2 - {R_i}^2\right)}{\left({R_d}^2 - {R_0}^2\right)\left({R_0}^2 - {R_i}^2\right)} \tag{A.35}$$

Similarly, the shear strain on the velocity discontinuity surface AL is calculated as:

$$\gamma_{\mathrm{AL}} = \frac{r^2 - {R_i}^2}{2rT} \tag{A.36}$$

Considering the dependency of shear strain on r on this surface, the average strain value in the range of r from R_i to R_0 is obtained as:

$$\gamma_{\mathrm{AL_{mean}}} = \frac{\left(\frac{{R_0}^2 - {R_i}^2}{2} + ln\frac{R_i}{R_0}\right)}{2T(R_0 - R_i)} \tag{A.37}$$

The effective strain for the shear components is calculated and summed as:

$$\bar{\varepsilon}_{(AE+AL)} = \sqrt{\frac{4}{3}{\gamma_{AE}}^2} + \sqrt{\frac{4}{3}{\gamma_{AL}}^2} \tag{A.38}$$

For the mentioned dimensions of the process, this strain is obtained as 2.9. The sum of this strain with the average strain values calculated for zones I and II equals the total strain applied to the material. This value is the sum of homogeneous and redundant strains applied to the material under frictionless conditions, based on the upper bound model. Thus, the difference between total and homogeneous strains equals the redundant strain applied to the material in the process, which depends on the upper bound model considered.

A.4. Internal Power Consumption

[DOI: 10.22068/ijmse.4600]

The average flow stress(σ_m) and shear stress (k_m) in each region, as well as the final shear stress (k_f), are calculated based on the average strains applied to the material as follows:

$$\sigma_{m_I} = \frac{\int_0^{\bar{\varepsilon}_I} K\varepsilon^n}{\varepsilon_I} \quad , \sigma_{m_{II}} = \frac{\int_{\bar{\varepsilon}_I}^{\bar{\varepsilon}_{II}+\bar{\varepsilon}_I} K\varepsilon^n}{\varepsilon_{II}}$$

$$k_{m_I} = \frac{\sigma_{m_I}}{\sqrt{3}} \quad , k_{m_{II}} = \frac{\sigma_{m_{II}}}{\sqrt{3}}$$

$$k_f = \frac{\sigma_f}{\sqrt{3}} = \frac{k(\bar{\varepsilon}_{II} + \bar{\varepsilon}_I)^n}{\sqrt{3}} \tag{A.39}$$

These values for the process dimensions are obtained as follows:

$$k_{m_I} = 46.19MPa \quad , k_{m_{II}} = 70.96MPa$$

$$k_0 = 22MPa$$

$$k_f = 78.51MPa$$

In regions *I* and *II*, internal deformation occurs. The first integral ($\frac{2}{\sqrt{3}}\sigma_0 \int_V \sqrt{\frac{1}{2}\dot{\varepsilon}_{ij}\dot{\varepsilon}_{ij}}\, dV$) over the volume of region *I* (V_I) and region *II* (V_{II}) is calculated as follows:

(A.40)

$$\dot{w}_{i_I} = \frac{2\pi\sigma_{m_I} v_p}{\sqrt{3}} \left[{R_d}^2 - \frac{{R_d}^2}{4} log(3) - \frac{\sqrt{3{R_0}^4 + {R_d}^4}}{2} - \frac{{R_d}^2}{4} log(\sqrt{3{R_0}^4 + {R_d}^4} - {R_d}^2) + \frac{{R_d}^2}{4} log(\sqrt{3{R_0}^4 + {R_d}^4} + {R_d}^2) \right]$$

$$\dot{w}_{i_{II}} = \frac{2\sigma_{m_{II}} C v_p \pi}{\sqrt{3}} \left[{}^1\!/_2 \sqrt{3R_0^4 + R_i^4} - \frac{R_i^2}{4} \; log(R_i^2 + \sqrt{3R_0^4 + R_i^4} + \frac{R_i^2}{4} log(\sqrt{3R_0^4 + R_i^4} - R_i^4) - R_i^2 + \frac{R_i^2}{4} log(3) \right]$$

[DOI: 10.22068/ijmse.4600]

A.5. Frictional Power on Interfaces

The frictional surfaces, as illustrated in Figure 1, include those with constant friction factor (m = 0.1)—namely, AB, BC, FL, LQ, and AP. The third integral in the power consumption equation (A. 41), formulated based on the upper-bound theorem originally proposed by Prager and Hodge [17] and subsequently modified and extended by Druker [18], is evaluated for these frictional surfaces as follows:

$$\dot{W}_{tot} = \frac{2}{\sqrt{3}}\sigma_0 \int_V \sqrt{\frac{1}{2}\dot{\varepsilon}_{ij}\dot{\varepsilon}_{ij}}\, dV + \int_{S_\Gamma} k|\Delta v_\Gamma|\, dS + \int_{S_f} mk|\Delta v_f|\, dS - \int_{Si} T_i v_i dS \tag{A.41}$$

For surface AB, the surface element is derived as follows, varying from R_0 to R_d. Also, we have $k = k_{m_I}$:

$$ds = 2\pi r dr \tag{A.42}$$

The velocity difference of the material on this surface is given by:

$$|\Delta v| = |v_{r_I}| = \frac{{R_d}^2 - r^2}{2rT} v_p \tag{A.43}$$

Thus, the power consumption on frictional surface AB is calculated as:

$$\dot{W}_{f_{AB}} = \frac{mk_{m_I} v_p \pi}{T}\left(\frac{{R_0}^3 + 2{R_d}^3}{3} - R_0 R_d^2\right) \tag{A.44}$$

For surface BC, the surface element is derived as follows, z varying from 0 to T. Also, we have $k = k_{m_I}$:

$$ds = 2\pi R_d dz \tag{A.45}$$

[DOI: 10.22068/ijmse.4600]

The velocity difference of the material on this surface is given by:

$$|\Delta v| = \left|v_{z_I}\right| = \frac{T - z}{T} v_p \tag{A.46}$$

Thus, the power consumption on frictional surface BC is calculated as:

$$\dot{W}_{f_{BC}} = m k_{m_I} \pi R_d v_p T \tag{A.47}$$

For surface FL, the surface element is derived as follows, z varying from 0 to T. Also, we have $k = k_{m_{II}}$:

$$ds = 2\pi R_i dz \tag{A.48}$$

The velocity difference of the material on this surface is given by:

$$\Delta v = \left|v_{z_{II}}\right| \tag{A.49}$$

Thus, the power consumption on frictional surface FL is calculated as:

$$\dot{W}_{f_{FL}} = m k_{m_{II}} C v_p \pi R_i T \tag{A.50}$$

For surface AP, the surface element is derived as follows, z varying from 0 to L_0 . Also, we have$k = k_f$:

$$ds = 2\pi R_0 dz \tag{A.51}$$

Considering that surface AP moves downward at speed $v_p$and the material slides on it with speed v_f in the opposite direction, the velocity difference of the material on this surface is given by:

$$|\Delta v| = v_p(1 + C) \tag{A.52}$$

Thus, the power consumption on frictional surface AP is calculated as:

[DOI: 10.22068/ijmse.4600]

$$\dot{W}_{f_{Ap}} = mk_f v_p(1+C)2\pi R_0 L_0 \tag{A.53}$$

For surface LQ, the surface element is derived as follows, z varying from 0 to L_{MN}. Also, we have $k = k_f$:

$$ds = 2\pi R_i dz \tag{A.54}$$

The velocity difference of the material on this surface is given by:

$$\Delta v = |v_f| = Cv_p \tag{A.55}$$

Thus, the power consumption on frictional surface LQ is calculated as:

$$\dot{W}_{f_{Lq}} = mk_f C v_p 2\pi R_i L_{MN} \tag{A.56}$$

A.6. Velocity Discontinuity Power

Discontinuity of velocity occurs on surfaces AE, AL, CE and EF, where the consumed energy is obtained from the second integral. For surface AE, the surface element is expressed as follows, and z varies from 0 to T

$$ds = 2\pi R_0 dz \tag{A.57}$$

The change in velocity occurring on this surface is given by:

$$|\Delta v| = v_{z_I} + v_{z_{II}} = \frac{T-z}{T} v_p(1+C) \tag{A.58}$$

Thus, the power consumption on this surface is obtained as:

$$\dot{W}_{v_{AE}} = k_{m_I}(1+C)v_p T\pi R_0 \tag{A.59}$$

[DOI: 10.22068/ijmse.4600]

For surface CE, the surface element is expressed as follows, varying from R_i to R_0. For surface CE, the surface element is derived as follows, r varying from R_0 to R_d. Also, we have $k = k_0$:

$$ds = 2\pi r dr \tag{A.60}$$

The velocity difference of the material on this surface is given by:

$$|\Delta v| = \left|v_{r_I}\right| = \frac{{R_d}^2 - r^2}{2rT} v_p \tag{A.61}$$

Thus, the power consumption on frictional surface CE is calculated as:

$$\dot{W}_{v_{CE}} = \frac{k_0 v_p \pi}{T}\left(\frac{2Rd^3 + R_0^3}{3} - R_d^2 R_0\right) \tag{A.62}$$

For surface EF, the surface element is derived as follows, r varying from R_i to R_0. Also, we have $k = k_0$:

$$ds = 2\pi r dr \tag{A.63}$$

The velocity difference of the material on this surface is given by:

$$|\Delta v| = \left|v_{r_{II}}\right| = C\frac{r^2 - {R_i}^2}{2rT} v_p \tag{A.64}$$

Thus, the power consumption on frictional surface EF is calculated as:

[DOI: 10.22068/ijmse.4600]

$$\dot{W}_{v_{EF}} = \frac{k_0 C \pi v_p}{T}\left[\left(\frac{2{R_i}^3 + {R_0}^3}{3} - R_i^2 R_0\right)\right] \quad \text{(A.65)}$$

For surface Al, the surface element is expressed as follows, varying from R_i to R_0.

$$ds = 2\pi r dr \quad \text{(A.66)}$$

The change in velocity occurring on this surface is given by:

$$|\Delta V| = v_{r_{II}} \quad \text{(A.67)}$$

Thus, the power consumption on this surface is obtained as:

$$\dot{W}_{v_{AL}} = \frac{k_f C v_p}{T}\left(\frac{{R^3}_0 + 2R_i^3}{3} - R_0 R_i^2\right) \quad \text{(A.68)}$$

A.7. Total Power and Extrusion Force

Total power input is the sum of internal, frictional, and discontinuity power. As we know, the total power consumed for deformation and the wasted powers must be supplied by the external force. The power applied by the external force can also be calculated from the product of the applied force and the speed of the punch movement. Therefore:

$$\dot{W}_{tot} = F.v_p = \pi\left({R_d}^2 - {R_0}^2\right)P_{Ext} v_p \quad \text{(A.69)}$$

Where P_{Ext} is the extrusion force applied on the punch. Using equation (69), the required pressure for extrusion can be easily calculated. This pressure is obtained as follows:

(A.70)

$$P_{ext} = \frac{\sigma_{m_I}}{\sqrt{3}(R_d^2 - R_0^2)}\left[2R_d^2 - R_d^2\, log\sqrt{3} - \sqrt{3R_0^4 + R_d^4} + \frac{R_d^2}{2} log\left(\frac{\sqrt{3R_0^4 + R_d^4} + R_d^2}{\sqrt{3R_0^4 + R_d^4} - R_d^2}\right)\right] +$$

[DOI: 10.22068/ijmse.4600]

$$\frac{\sigma_{m_{II}}}{\sqrt{3}(R_0^2-R_i^2)}\left[-2R_i^2+R_i^2\,log\sqrt{3}+\sqrt{3R_0^4+R_i^4}+\frac{R_i^2}{2}log(\frac{\sqrt{3R_0^4+R_i^4}-R_i^2}{\sqrt{3R_0^4+R_i^4}+R_i^2})\right]+$$

$$\frac{1}{R_d^2-R_0^2}\left[\begin{matrix}R_0(1+C)(k_{m_I}T+2mk_fL_0)+\frac{(mk_{m_I}+k_0)}{T}(\frac{R_0^3+2R_d^3}{3}-R_0R_d^2)+mK_{m_I}R_dT+\\ mK_{m_{II}}CR_iT+2mK_fCR_iL_{MN}\end{matrix}\right]$$

$$+\frac{1}{T(R_0^2-R_i^2)}\left(\frac{R_0^3+2R_i^3}{3}-R_0R_i^2\right)(K_f+K_0)$$

For the given geometry and process parameters, the solution of $\frac{\partial}{\partial T}(P_{Ext})=0$ the depth of the deformation region is obtained as follows:

(A.71)

$$T^2=\left[\frac{(R_d{}^2-R_0^2)\frac{\left(\frac{R_0^3+2R_i{}^3}{3}-R_0R_i^2\right)(k_f+k_0)}{(R_0^2-R_i^2)}+\frac{\left(\frac{R_0^3+2R_d{}^3}{3}-R_0R_d^2\right)(mk_{m_I}+k_0)}{(R_d^2-R_0^2)}}{\left(\frac{mk_{m_{II}}(R_d^2-R_0^2)Ri}{(R_0^2-R_i^2)}+mk_{m_I}R_d+k_{m_I}R_0\left(1+\frac{R_d^2-R_0{}^2}{R_0^2-R_i^2}\right)\right)}\right]$$

[DOI: 10.22068/ijmse.4600]